Archean seafloors shallowed with age due to radiogenic heating in the mantle

Juan Carlos Rosas[1,2,*], Jun Korenaga[1]

[1]Department of Earth and Planetary Sciences, Yale University

P.O. Box 208109, New Haven, CT 06520-8109, USA

[2]Departamento de Geofísica Aplicada,

Centro de Investigación Científica y de Educación Superior de Ensenada

Carretera Tijuana-Ensenada No. 3918, Zona Playitas, Ensenada, Baja California,

C.P. 22860, México

[*]Corresponding author

Email addresses: juanrb@cicese.mx (Juan Carlos Rosas), jun.korenaga@yale.edu (Jun Korenaga)

Given the scarcity of geological data, knowledge of Earth's landscape during the Archean is limited. Although the continental crust may have been as massive as present by 4 Ga, the extent to which it was submerged or exposed is unclear. One key component in understanding the amount of exposed landmasses in the early Earth is the evolution of the oceanic lithosphere. Whereas the present-day oceanic lithosphere subsides as it ages, based on numerical models of mantle convection we find that higher internal heating due to a larger concentration of radioactive isotopes in the Archean mantle halted subsidence, possibly inducing seafloor shallowing prior to 2.5 Ga. In such a scenario, exposed landmasses in the form of volcanic islands and resurfaced seamounts or oceanic plateaus can remain subaerial for extended periods of time, and may have provided the only stable patches of dryland in the Archean. Our results therefore permit a reevaluation of possible locations for the origin of life, as they provide support to existing hypothesis that suggests that life had its origins on land rather than in an oceanic environment.

Nucleobases were either formed under early Earth conditions [1, 2, 3] or had an extraterrestrial origin [4]. The synthesis of complex biomolecules capable of self-replication, however, involves polymerization of nucleobases into nucleotides and nucleic acids. Because polymerization requires precise thermodynamic conditions [5, 6, 7] that were unlikely to be prevalent in the early Earth, an understanding of the Archean surface environment is essential when discussing possible locations for abiogenesis. Presently, candidate locations include deep-sea hydrothermal vents [8] or warm little ponds near volcanic flanks [9]. Phylogenetic studies have suggested that hyperthermophilic archaea of the type found near the vents may be akin to the last universal common ancestor, suggesting that life might have arisen in these vents [10]. However, hyperthermophiles may just be survivors of bolide impacts in the early Earth [11], and the capacity of the vents and surroundings to sustain polymerization is still debated [5, 6, 7]. Warm little ponds, in turn, allow for long-term polymerization through seasonal wet-dry and/or freeze-thaw cycles [12, 13, 14] but require the existence of exposed landmasses [15, 16].

Given a limited number of geological constraints, estimating the extent of exposed landmass during the Archean is difficult. A recent theoretical study that considers the co-evolution of prebiotic chemistry and surface environment suggests polymerization in warm little ponds following the delivery of nucleotides by meteorites [17]. Their parameterization of exposed landmass in the Archean is, however, questionable because it assumes that the mass of exposed continents is equal to the mass of continental crust. Although it is possible that continents were as massive as present by 4 Ga [18, 19], the amount of exposed landmass is a function of several time-dependent parameters, such as ocean-mantle water exchange and seafloor topography [20]. In particular, seafloor topography in deep time is poorly understood. As newly-formed seafloor moves away from a mid-ocean ridge, isostatic adjustment due to cooling from the surface results in changes in seafloor depth [21], thus affecting the water capacity of ocean basins and the flooding of continents. At present, volcanic islands become seamounts owing to continuous seafloor subsidence (Figure 1a). Subsidence then appears to slows down when the lithosphere is 70-80 Myr-old, likely owing to the onset of small-scale convection [22] as well as the impingement of mantle plumes [23]. In the Archean, however, radiogenic heat production in the mantle was approximately four times larger than at present [24]. If radiogenic heating is high enough, subsidence may cease altogether and seafloor shallowing might occur, allowing seamounts and oceanic plateaus to resurface (Figure 1b).

To assess the likelihood of exposed landmasses in the Archean, therefore, we systematically explore the effect of radiogenic heating on bathymetry through numerical modeling. As shown later, our results suggest that seafloor shallowing is indeed possible for the bulk of the Archean. Additionally, we also explore the effect of our new model of bathymetric evolution on the sea level, mid-ocean ridge depth, and the exposed fraction of continental crust, thus providing a more comprehensive assessment of the Archean landscape and its possible implications for the origin of life.

Modeling seafloor bathymetry

To model the evolution of seafloor topography, we integrate the two-dimensional (2-D) thermal convection equations with temperature-dependent viscosity and radiogenic heating using a finite-element approach [25]. The running time is 500 Myr. Our strategy consists in calculating 2-D ridge-parallel thermal evolution and then horizontally averaging such evolution to construct a 2-D, ridge-perpendicular, mantle thermal structure with a prescribed plate velocity [26] (see Methods; Extended Data Figure 1). Instantaneous Stoke flow is then computed for this mantle structure. Seafloor depth is calculated as:

$$w = \left(\alpha \Delta T d \frac{\rho_m}{\rho_m - \rho_w}\right) \frac{\sigma^*_{zz}|_{z^*=0}}{Ra}, \tag{1}$$

where w is subsidence with respect to zero-age seafloor, α is thermal expansivity (set as 3×10^{-5} K^{-1}), ΔT is mantle potential temperature (1350 K at present), d is mantle thickness (2900 km), ρ_m is surface mantle density (3300 kg m^{-3}), ρ_w is density of water (1000 kg m^{-3}), $\sigma^*_{zz}|_{z^*=0}$ is the nondimensional normal stress at the surface, and $Ra = \alpha\rho_0 g \Delta T d^3/\eta_0\kappa$ is the Rayleigh number, for which ρ_0 is reference density (4000 kg m^{-3}), κ is thermal diffusivity (10^{-6} m^2 s^{-1}), g is gravitational acceleration (9.8 m s^{-2}), and η_0 is the reference asthenospheric viscosity. We vary η_0 within the range 10^{19}-10^{20} Pa s, consistent with geophysical observations [27]; we assume that the present-day asthenospheric viscosity is also valid for the Archean, based on the likely effect of global water cycle on mantle viscosity [28]. The viscosity structure of the mantle is computed using realistic temperature dependence with an activation energy of 300 kJ mol^{-1} (see Methods).

We measure the effect of radiogenic heating by varying the heating rate per unit mass, H, and comparing the subsidence with that predicted by the case with H=0. Prior to the onset of sublithospheric convection, the latter case is equivalent to seafloor subsidence as predicted by the half space cooling (HSC) model with no radiogenic heating:

$$w_{\text{hs}} = 2\alpha\Delta T d \frac{\rho_m}{\rho_m - \rho_w}\left(\frac{\kappa\tau}{\pi}\right)^{1/2}, \tag{2}$$

where τ is the age of the lithosphere [21]. The range of H is from 2.1×10^{-12} W kg^{-1} at present to 8.5×10^{-12} W kg^{-1} at the Hadean-Archean boundary (4 Ga), as calculated from the present concentrations of K (102 ppm), U (9.7 ppb) and Th (30 ppb) in the depleted mantle [24].

Effect of radiogenic heating and mantle viscosity on seafloor bathymetry

Seafloor bathymetry is most sensitive to radiogenic heating, with $H > 0$ leading to slower seafloor subsidence than that predicted by the HSC model (Figure 2a-c). Significant shallowing is inferred from our model throughout the Archean, starting at $\sim$50-100 Myr. As H decreases, shallowing also decreases, and by 1.7 Ga the seafloor is continuously subsiding. On the contrary, whereas variations in asthenospheric viscosity have a noticeable effect on the onset of sublithospheric convection (with decreasing viscosity leading to an earlier onset time), the overall evolution of a subsidence curve for a given H does not change significantly when the viscosity is in the range of 10^{19}-10^{20} Pa s, suggesting seafloor shallowing probably occurred in the early Earth regardless of the value of η_0.

More realistic models may be explored by employing depth-dependent profiles for heat generation and viscosity. Depth-dependent heat generation results from the melting of the mantle, which partitions heat-producing elements into the oceanic crust. We employ depleted mantle concentrations of K, U and Th, as before, from which we calculate three profiles for three ages: present, 2.5 Ga and 4 Ga (Figure 2d). For each case, we assume that all heat-producing elements partition into the crust, leaving behind an entirely depleted (H=0) mantle lithosphere. The concentration of heat-producing elements in the crust is calculated from the expected thicknesses for the crust and the mantle lithosphere at each age (7 km and 70 km, respectively, at present, 29 km and 137 km at 2.5 Ga, and 19 km and 106 km at 4 Ga, as calculated from the thermal history of the upper mantle [29] and a mantle melting model [30]). For the viscosity profile, several geophysical observations suggest that the lower mantle may be ∼10-30 times more viscous, on average, than the upper mantle [27]. We constructed two viscosity profiles with a tenfold and thirtyfold increase in lower mantle viscosity, in addition to the purely temperature-dependent case (Figure 2e). For the asthenospheric viscosity, we employ $\eta_0 \sim 3 \times 10^{19}$ Pa s.

For a given age, bathymetry for models with depth-dependent H is roughly comparable to that predicted by models with uniform H (Figure 2f). This suggests that dynamic topography reflects the aggregated heat content in the subsurface, thereby being insensitive to the details of vertical distribution; this is consistent with the topography kernel (the sensitivity of topography to the internal density structure) expected for the suboceanic mantle [31]. The lower-mantle viscosity partially modulates the effect of radiogenic heating on bathymetry. At low H, the model is mostly cooling from above and density changes are located within the lithosphere only. Dynamic topography thus remains insensitive to the viscosity structure of the convective interior. As H increases, however, the effect of the viscosity of the lower mantle becomes noticeable. A general trend is that a higher value of lower-mantle viscosity consistently gives deeper seafloor, although the difference introduced by the thirtyfold increase in the lower mantle is < 1 km at most in the Hadean-Archean boundary. This trend is also consistent with how the topography kernel is influenced by depth-dependent viscosity [31]. Overall, using depth-dependent profiles of heat generation and viscosity does not significantly affect the bathymetry with respect to models with uniform profiles.

Archean surface environment and the origin of life

The models above highlight the effect of radiogenic heating on seafloor depth. Moreover, the high concentration of heat-producing elements in the early mantle suggest that seafloor shallowing was possible prior to 2.5 Ga. We now model the Archean surface environment by tracking the evolution of sea level, ridge depth, and the exposed fraction of continents. For this, we use a recent freeboard model developed to investigate the global water cycle [20].

Our freeboard model assumes isostatic balance across ocean basins and continents. Secular changes in continental lithospheric buoyancy are allowed [32], as well as changes in seafloor bathymetry through either HSC bathymetry or the bathymetry with radiogenic heating (hereafter referred to as RH bathymetry). To facilitate modeling, we parameterize the RH bathymetry through an empirical scaling law for w, expressed as a function of H (see Methods; equation 16 and Extended Data Figures 2-3). Our modeling strategy closely follows that of Ref. [20], but the following two input parameters are worth some detailed account: (1) the continental growth function, and (2) the ocean-mantle water flux due to subduction.

The growth of continents is parameterized through:

$$M_c(t) = \frac{M_c(t_p)}{1 - \mathrm{e}^{-\kappa_g(t_p - t_s)}}\left[1 - \mathrm{e}^{-\kappa_g(t-t_s)}\right], \tag{3}$$

where M_c is the continental mass, t_s is the time when crustal growth started (4.51 Ga), t_p is the present time measured from the beginning of the solar system (4.567 Ga), $M_c(t_p)$ is the present continental mass (2.09×10^{22} kg), and κ_g is a growth constant [18]. By adjusting κ_g, we can explore a wide range of crustal growth scenarios. We test two models: $\kappa_g = 17$, representing a rapid continental growth in the Hadean, and $\kappa_g = 0.5$, representing a gradual growth of the continents (Figure 3a). The rapid growth model is consistent with the evolution of the samarium-neodymium isotope systems [18] as well as the degassing history of argon [19]. The gradual growth model is tested here to assess the effects of growth rate on landscape evolution. As for the ocean-mantle water flux, we constrain it by selecting a constant value that keeps the sea level approximately stable up to 2.5 Ga, consistent with the geological record [20, 33]. Net water flux in the ocean-mantle system has various sources and sinks, including water loss by subducting slabs (in sediments, the crust and lithospheric mantle), magmatic output from mid-ocean ridges, hotspots, and arcs, and non-magmatic up-dip transport from slab to oceans. Considerable uncertainties exist even when estimating the present-day water flux [34, 35]. Yet, using a constant value of net water influx is justified a posteriori, as a long-term average that can reproduce a steady sea level, at least back to 2.5 Ga. It should be stressed that, even with non-zero water flux, sea level can remain constant owing to changes in the relative buoyancy of continental lithosphere with respect to that of oceanic lithosphere [20, 32]. Positive net water flux indicates more voluminous oceans in the past. Other model parameters are the same as in the reference case of the original freeboard study [20]. For the models presented here, we assume the continuous operation of plate tectonics [28] with a decrease in plate velocity in the past. With the effect of mantle melting on viscosity (i.e., dehydration stiffening), a hotter mantle in the past is expected to convect more slowly, thus leading to slower plate tectonics [30]. Such a dynamics has been shown to be consistent with a range of geological records including the life spans of passive margins [36], the cooling history of the upper mantle [29], and the evolution of continental plate velocities [37, 38].

Most studies place the present net ocean-mantle water flux at $< 10 \times 10^{14}$ g yr^{-1} [20, 34, 35, 39, 40], although it could be as large as 18×10^{14} g yr^{-1} [35]. In this study, 3.3×10^{14} g yr^{-1} and 4.4×10^{14} g yr^{-1} are required to satisfy the constancy of sea level from 2.5 Ga to present for the rapid and gradual growth models, respectively (Figures 3b-c), in relative agreement with the most recent estimates [20, 39]. With these fluxes, ridge depth was deeper in the past (Figures 4a and 4e). Continents become more flooded with RH bathymetry than with HSC bathymetry because the former leads to shallower seafloor, and thus a higher sea level (Figures 4b and 4f). Additionally, a more gradual growth of continents means that the ocean basins would have been wider in the past, being able to hold more water and resulting in less continental flooding.

Hypsometry snapshots through the Archean and at present are shown in Figures 4c-d for RH bathymetry. During the early Archean, as the tempo of plate tectonics was slower [20, 28], the maximum age of oceanic lithosphere is extended and seafloor flattening is more likely to occur. By 2.5 Ga, flattening is still appreciable. For the present-day case, because the bathymetry is better approximated by the plate cooling model [41], we also consider this case. For both growth models, the RH and plate model hypsometries are approximately equal, indicating the accuracy of our approach. In comparison, using HSC bathymetry results in continuous seafloor subsidence throughout the Archean (Figures 4g-h).

Although the chosen model for continental growth does have an impact on the size of ocean basins and thus on sea level, seafloor shallowing occurs for both rapid and gradual growth. This result is particularly important; because the rapid and gradual growth models could be considered end-member scenarios for other intermediate growth models that have been proposed [42], seafloor shallowing in the Archean is expected to persist regardless of the details of continental formation. The results presented here, therefore, are robust enough to provide a picture of an Archean landscape in which the seafloor shallows up and submerged seamounts and oceanic plateaus may resurface (Figure 1).

The existence of dryland in the Archean is compatible with a number of origin-of-life models [14, 15], and the results presented here provide geological support to such theories. Unequivocal evidence of life has been dated at 3.5 Ga [43], although the record may be pushed back to the late Hadean or early Archean ($\sim$4 Ga) [44]. During this period, our results indicate that continents were fully submerged (Figures 4b and 4f). As we assume a time-independent water influx, this part of our modeling results is subject to greater uncertainties compared to the Proterozoic part. The mantle at $>$2.5 Ga is likely to have been hotter than that at $<$2.5 Ga [29], and net water influx can be more reduced in the Archean [39]. Even if the net water influx is reduced in half during the Archean, however, continents are still expected to have been fully submerged (Figure 3b,c). Also, temporal topographic elevation by continent-continent collision is expected to be limited because of hot crustal geotherm in the Archean [45], and this effect is already included in our freeboard modeling [20]. This may be used to argue that the synthesis of the first prebiotic compounds likely occurred in an aquatic environment, such as near hydrothermal vents. The formation of primitive RNA-like molecules, however, requires polymerization of nucleotides [46], and the vent's surroundings are probably not well suited for this. High water temperature near the vents [5] and low concentration of phosphorous compounds and nitrogen oxides in the primitive ocean [6, 7] are considered to be limiting factors. The very presence of water may also be problematic, because water tends to degrade polymerization and inhibit the formation of nucleotides through hydrolysis. Although it is possible for polymers to form with the aid of mineral surfaces [47] or within pore space near the vents [48], the results we present here permit us to consider warm little ponds as an alternative location. The synthesis of organic compounds is achievable in these ponds through wet-dry and freeze-thaw cycles [13, 14], or through geochemical reactions such as serpentinization of ultramafic igneous rocks [15]. Even with continents submerged, seafloor shallowing due to radiogenic heating would ensure that any volcanic islands formed on sufficiently old seafloor or resurfaced seamounts and oceanic plateaus would be long-lived (Figure 1b), providing the exposed landmass that is required for warm little ponds to exist. What is promising about this new possibility is that, whereas the spatial extent of such oceanic islands and plateaus may be limited, the tendency of these landmasses to remain subaerial is robust, as it is supported by the long-term mantle-scale heating. Considering the thermodynamic limitations of deep-water hydrothermal vents as a possible site for abiogenesis, therefore, the results presented here suggest that warm little ponds are a viable location for the origin of life.

Methods

Model Description

All models share the following boundary conditions and properties. Surface temperature is set to zero and the bottom boundary is insulated. The top and bottom boundaries are free slip, and a reflecting boundary condition is applied to the sides. Time and temperature are nondimensionalized by d^2/κ and ΔT, respectively, where d is model depth, κ is thermal diffusivity and ΔT is the difference between initial and surface temperature. Nondimensional variables are denoted with an asterisk. The aspect ratio is set to 4, and the model is discretized into 257 horizontal and 93 vertical nodes. Whereas the horizontal nodes are distributed uniformly, we concentrate 40 of the 93 vertical nodes in the shallowest part of the model ($z^*\geq 0.8$, where z^* is height and $z^*=1$ is the top surface) to better capture the dynamics of sublithospheric convection (i.e., growth and instability of the upper thermal boundary layer).

We employ a linearized version of the Arrhenius-type of temperature-dependent viscosity, given by:

$$\eta^*(T^*) = \exp\left[\theta(1 - T^*)\right], \tag{4}$$

where η^* is normalized by reference (i.e. asthenospheric) viscosity, η_0, defined at $T^*=1$, and θ is the Frank-Kamenetskii parameter [49], which is related to the activation energy, E, as:

$$\theta = \frac{E\Delta T}{R(T_s + \Delta T)^2}, \tag{5}$$

where R is the universal gas constant and T_s=273 K is the surface temperature. The Rayleigh number is defined as:

$$Ra = \frac{\alpha\rho_0 g\Delta T d^3}{\eta_0\kappa}, \tag{6}$$

where α is thermal expansivity (3×10^{-5} K^{-1}), ρ_0 is reference density (4000 kg m^{-3}), and g is gravitational acceleration (9.8 m s^{-2}). Finally, heat generation rate per unit mass (H) is nondimensionalized by:

$$H^* = \left(\frac{\rho_0 d^2}{k\Delta T}\right) H, \tag{7}$$

where k=4 W m^{-1} K^{-1} is thermal conductivity.

Our models are fully described by the three non-dimensional parameters θ, Ra and H^*. We employ $\theta = 18.5$ for all our models, consistent with $E = 300$ kJ mol^{-1} for the upper mantle [50]. Such a value for θ remains approximately constant in the deep time because of the limited variation of ΔT (1350 K at present). The asthenospheric viscosity is set between 10^{19} Pa s and 10^{20} Pa s, corresponding to $Ra \sim 3 \times 10^8 - 3 \times 10^9$. The range of H^* is between 0 and 50, corresponding to $H = 0 - 8.5 \times 10^{-12}$ W kg^{-1} (see Theoretical Formulation and Results). Because the bottom boundary is insulated, our models are purely internally-heated and do not incorporate the effect of upwelling mantle plumes, thus allowing us to focus on the dynamics of the ocean lithosphere exclusively.

Our modeling strategy is as follows [26]. We run a convection model for a given set of Ra and H^* for a duration of 500 Myr. Depth-dependent profiles for H^* and viscosity (see Figures 2d-e) may also be employed. At each time step, we calculate an horizontally-averaged temperature profile from 2-D ridge-parallel simulation (Extended Data Figures 1a-c) and assemble them to create a ridge-perpendicular thermal structure profile with a prescribed plate velocity (Extended Data Figure 1d). Instantaneous Stokes flow is then computed. Dynamic seafloor topography (i.e. topography due to mantle motions) along our trench-perpendicular thermal structure is proportional to the normal stress acting on the surface, $\sigma_{zz}|_{z=0}$:

$$\sigma_{zz}|_{z=0} = \alpha\rho_0 g w. \tag{8}$$

Equation (1) may then be obtained by nondimensionalizing the normal stress by $\eta_0\kappa/d^2$ in Equation (8), and multiplying by the topographic scale $\alpha\Delta T d\rho_m/(\rho_m - \rho_w)$. Seafloor subsidence is then converted to a function of seafloor age using the prescribed plate velocity. It should be noted that Equation (1), when applied to a model with $H = 0$, recovers the bathymetry predicted by the half space cooling model (Equation 2).

Empirical Scaling Law for Seafloor Subsidence

To apply our model of bathymetric evolution to our freeboard model, however, we develop an empirical scaling law for seafloor subsidence by using the results from our generic models (Extended Data Figure 2) and analyzing the deviation of modeled seafloor depth (w; equation 1) with respect to the seafloor depth as calculated from the HSC model (w_{hs}; equation 2). We define this deviation as:

$$\delta w = \frac{w_{\mathrm{hs}} - w}{w_{\mathrm{hs}}}. \tag{9}$$

Seafloor depth deviates from that predicted by the HSC model as internal heating increases (Extended Data Figure 2a). Because sublithospheric convection affects subsidence after the onset time (t_c), we construct our empirical scaling law by approximating the evolution of δw during the conductive (i.e., prior to onset time) and convective phases through linear trends. For the conductive phase, the linear trend is given by:

$$\delta w_1 = m_1(t^{1/2} - t_i^{1/2}), \tag{10}$$

where m_1 is the slope and $t_i^{1/2} \approx 2.5$ Myr$^{1/2}$ is the intersection with the horizontal axis (Extended Data Figure 2a). The subscript 1 refers to the conductive phase. The slope is a function of H^* (Extended Data Figure 2b), and it may be found from the following linear fit:

$$m_1 = a_1 H^*. \tag{11}$$

where $a_1 = 0.001$. Substituting equations (9) and (11) into equation (10), the empirical scaling law for the seafloor subsidence during the conductive phase is given by:

$$w_1 = w_{\mathrm{hs}} \Big[1 - a_1 H^* (t^{1/2} - t_i^{1/2}) \Big]. \tag{12}$$

Similarly, the linear trend for the evolution of δw after the onset of convection is given by:

$$\delta w_2 = \delta w_1(t_c) + m_2(t^{1/2} - t_c^{1/2}), \tag{13}$$

where the subscript 2 refers to the convective phase, and the slope m_2 is given by:

$$m_2 = \frac{\delta w_2(t_{\max}) - \delta w_1(t_c)}{t_{\max}^{1/2} - t_c^{1/2}}. \tag{14}$$

In equation (14), the maximum running time is set at $t_{\max} = 500$ Myr. For $\delta w_2(t_{\max})$, we notice that the final seafloor depth for a given amount of radiogenic heating is approximately the same for all reference viscosity (i.e., Rayleigh number) values (Figure 2a-c). We can thus express $\delta w_2(t_{\max})$ as a function of H^* only (Extended Data Figure 2c), and the data may be fitted by:

$$\delta w_2(t_{\max}) = a_2 H^* + b_2, \tag{15}$$

where $a_2 = 0.0228$ and $b_2 = 0.0452$. We may find δw_2 from equations (12)-(15). Our empirical scaling law for seafloor subsidence throughout 500 Myr (w_s) is thus a piecewise function of the form:

$$w_s = w_{\text{hs}} \times \begin{cases} 1 - a_1 H^*(t^{1/2} - t_i^{1/2}) & , t < t_c \\ 1 - a_1 H^*(t_c^{1/2} - t_i^{1/2}) + \dfrac{H^*\left[a_1(t_c^{1/2} - t_i^{1/2}) - a_2\right] - b_2}{t_{\max}^{1/2} - t_c^{1/2}}\left(t^{1/2} - t_c^{1/2}\right) & , t_c \leq t \leq t_{\max}, \end{cases} \tag{16}$$

where t_c may be calculated from previously derived scaling laws [25].

The difference between the subsidence as calculated from equation (1) and through our empirical scaling remains relatively low (below 250 m) for all values of Ra and H^* (Extended data Figure 3). Because our empirical scaling is based on the analytical HSC bathymetry model, seafloor subsidence may be readily calculated for any given value of radiogenic heating through equation (16), allowing us to bypass the instantaneous Stokes flow calculation on which our modeling results are constructed.

References

[1] Miller, S. L. A production of amino acids under possible primitive Earth conditions. *Science* **117**, 528-529 (1953).

[2] Lazcano, A. & Bada, J. L. The 1953 Stanley L. Miller experiment: Fifty years of prebiotic organic chemistry. *Origins of life and evolution of the biosphere* **33**, 235-242 (2003).

[3] Bada, J. L. New insights into prebiotic chemistry from Stanley Miller's spark discharge experiments. *Chemical Society Reviews* **42**, 2186-2196 (2013).

[4] Chyba, C. & Sagan, C. Endogenous production, exogenous delivery and impact-shock synthesis of organic molecules: an inventory for the origins of life. *Nature* **355**, 125-132 (1992).

[5] Miller, S. L. & Bada, J. L. Submarine hot springs and the origin of life. *Nature* **334**, 609-611 (1988).

[6] Mulkidjanian, A. Y., Bychkov, A. Y., Dibrova, D. V., Galperin, M. Y. & Koonin, E. V. Origin of first cells at terrestrial, anoxic geothermal fields. *Proceedings of the National Academy of Sciences* **109**, E821-E830 (2012).

[7] Ranjan, S., Todd, Z. R., Rimmer, P. B., Sasselov, D. D. & Babbin, A. R. Nitrogen oxide concentrations in natural waters on early Earth. *Geochemistry, Geophysics, Geosystems* **20**, 2021-2039 (2019).

[8] Martin, W., Baross, J., Kelley, D. & Russell, M. J. Hydrothermal vents and the origin of life. *Nature Reviews Microbiology* **6**, 805-814 (2008).

[9] Peretó, J., Bada, J. L. & Lazcano, A. Charles Darwin and the origin of life. *Origins of Life and Evolution of Biospheres* **39**, 395-406 (2009).

[10] Weiss, M. et al. The physiology and habitat of the last universal common ancestor. *Nature Microbiology* **1**, 16116 (2016).

[11] Sleep, N. H. Geological and geochemical constraints on the origin and evolution of life. *Astrobiology* **18**, 1199-1219 (2018).

[12] Benner, S. A., Kim, H. J. & Carrigan, M. A. Asphalt, water, and the prebiotic synthesis of ribose, ribonucleosides, and RNA. *Accounts of Chemical Research* **45**, 2025-2034 (2012).

[13] Mutschler, H., Wochner, A. & Holliger, P. Freeze-thaw cycles as drivers of complex ribozyme assembly. *Nature Chemistry* **7**, 502-508 (2015).

[14] Damer, B. A field trip to the Archaean in search of Darwin's warm little pond. *Life* **6**, 21 (2016).

[15] Benner, S. A., Kim, H. J., Kim, M. J. & Ricardo, A. Planetary organic chemistry and the origins of biomolecules. *Cold Spring Harbor Perspectives in Biology* **2**, a003467 (2010).

[16] Bada, J. L. & Korenaga, J. Exposed areas above sea level on Earth >3.5 Gyr ago: Implications for prebiotic and primitive biotic chemistry. *Life* **8**, 55 (2018).

[17] Pearce, B. K. D., Pudritz, R. E., Semenov, D. A. & Henning, T. K. Origin of the RNA world: The fate of nucleobases in warm little ponds. *Proceedings of the National Academy of Sciences* **114**, 11327-11332 (2017).

[18] Rosas, J. C. & Korenaga, J. Rapid crustal growth and efficient crustal recycling in the early Earth: Implications for Hadean and Archean geodynamics. *Earth and Planetary Science Letters* **494**, 42-49 (2018).

[19] Guo, 329 M. & Korenaga, J. Argon constraints on the early growth of felsic continental crust. *Science Advances* **6**, 21 (2020).

[20] Korenaga, J., Planavsky, N. J. & Evans, D. A. D. Global water cycle and the coevolution of the Earth's interior and surface environment. *Philosophical Transactions of the Royal Society A* **375**, 20150393 (2017).

[21] Turcotte, D. L. & Schubert, G. *Geodynamics* (Cambridge University Press, Cambridge, 2002).

[22] Parsons, B. & McKenzie, D. Mantle convection and the thermal structure of the plates. *Journal of Geophysical Research* **83**, 4485-4496 (1978).

[23] Sleep, N. H. Small-scale convection beneath oceans and continents. *Chinese Science Bulletin* **56**, 1292-1317 (2011).

[24] Korenaga, J. Pitfalls in modeling mantle convection with internal heat production. *Journal of Geophysical Research* **122**, 4064-4085 (2017).

[25] Korenaga, J. & Jordan, T. H. Physics of multiscale convection in Earth's mantle: Onset of sublithospheric convection. *Journal of Geophysical Research* **108**, 2333 (2003).

[26] Korenaga, J. Seafloor topography and the thermal budget of Earth. In *The Interdisciplinary Earth: A Volume in Honor of Don L. Anderson*, 167-185 (Geological Society of America, 2015).

[27] Hager, B. Mantle viscosity: a comparison of models from postglacial rebound and from the geoid, plate driving forces, and advected heat flux. In *Glacial isostasy, sea level and mantle rheology*, 493-513 (American Geophysical Union, 1991).

[28] Korenaga, J. Initiation and evolution of plate tectonics on Earth: Theories and observations. *Annual Review of Earth and Planetary Sciences* **41**, 117-151 (2013).

[29] Herzberg, C., Condie, K. & Korenaga, J. Thermal history of the Earth and its petrological expression. *Earth and Planetary Science Letters* **292**, 79-88 (2010).

[30] Korenaga, J. Archean geodynamics and the thermal evolution of Earth. In *Archean Geodynamics and Environments*, 7-32 (American Geophysical Union, 2006).

[31] Korenaga, T. & Korenaga, J. Evolution of young oceanic lithosphere and the meaning of seafloor subsidence rate. *Journal of Geophysical Research* **121**, 6315-6332 (2016).

[32] Servali, A. & Korenaga, J. Oceanic origin of continental mantle lithosphere. *Geology* **46**, 1047-1050 (2018).

[33] Bindeman, I. N. et al. Rapid emergence of subaerial landmasses and onset of a modern hydrologic cycle 2.5 billion years ago. *Nature* **557**, 545-548 (2018).

[34] Ito, E., Harris, D. M. & Anderson, A. T. Alteration of oceanic crust and geologic cycling of chlorine and water. *Geochimica et Cosmochimica Acta* **47**, 1613-1624 (1983).

[35] Jarrard, R. D. Subduction fluxes of water, carbon dioxide, chlorine, and potassium. *Geochemistry, Geophysics, Geosystems* **4**, 5 (2003).

[36] Bradley, D. C. Passive margins through earth history. *Earth-Science Reviews* **91**, 1-26 (2008).

[37] Condie, K., Pisarevsky, S. A., Korenaga, J. & Gardoll, S. Is the rate of supercontinent assembly changing with time? *Precambrian Research* **259**, 278-289 (2015).

[38] Pehrsson, S. J., Eglington, B. M., Evans, D. A. D., Huston, D. & Reddy, S. M. Metallogeny and its link to orogenic style during the Nuna supercontinent cycle. In *Supercontinent Cycles Through Earth History* (Geological Society of London, 2016).

[39] Magni, V., Bouilhol, P. & van Hunen, J. Deep water recycling through time. *Geochemistry, Geophysics, Geosystems* **15**, 4203-4216 (2014).

[40] van Keken, P. E., Hacker, B. R., Syracuse, E. M. & Abers, G. A. Subduction factory: 4. Depth-dependent flux of H_2O from subducting slabs worldwide. *Journal of Geophysical Research* **116**, B1 (2011).

[41] Stein, C. A. & Stein, S. A model for the global variation in oceanic depth and heat flow with lithospheric age. *Nature* **359**, 123-129 (1992).

[42] Korenaga, J. Crustal evolution and mantle dynamics through Earth history. *Philosophical Transactions of the Royal Society A* **376**, 20170408 (2018).

[43] Walter, M. R., Buick, R. & Dunlop, J. S. R. Stromatolites 3,400-3,500 Myr old from the North Pole area, Western Australia. *Nature* **284**, 443-445 (1980).

[44] Bell, E. A., Boehnke, P., Harrison, T. M. & Mao, W. L. Potentially biogenic carbon preserved in a 4.1 billion-year-old zircon. *Proceedings of the National Academy of Sciences* **112**, 14518-14521 (2015).

[45] Rey, P. F. & Houseman, G. Lithospheric scale gravitational flow: the impact of body forces on orogenic processes from Archaean to Phanerozoic. G*eological Society, London, Special Publications* **253**, 153-167 (2006).

[46] Deamer, D. W. & Georgiou, C. D. Hydrothermal conditions and the origin of cellular life. *Astrobiology* **15**, 1091-1095 (2015).

[47] Burcar, B. T. et al. RNA oligomerization in laboratory analogues of alkaline hydrothermal vent systems. *Astrobiology* **15**, 509-522 (2015).

[48] Baaske, P. et al. Extreme accumulation of nucleotides in simulated hydrothermal pore systems. *Proceedings of the National Academy of Sciences* **104**, 9346-9351 (2007).

[49] Solomatov, V. S. & Moresi, L. N. Scaling of time-dependent stagnant lid convection: Application to small-scale convection on Earth and other terrestrial planets. *Journal of Geophysical Research* **105**, 21795-21817 (2000).

[50] Karato, S. & Wu, P. Rheology of the upper mantle: a synthesis. *Science* **260**, 771-778 (1993).

Acknowledgments

The authors are grateful to Karyn Rogers, Loren Williams and Ricardo Hernandez for their help and assistance while preparing this manuscript, and to Norman Sleep for comments on an earlier version of the manuscript. This material is based upon work supported in part by two grants from the U.S. National Aeronautics and Space Administration: (1) through the NASA Astrobiology Institute under Cooperative Agreement No. NNA15BB03A, and

(2) under Cooperative Agreement No. 80NSSC19M0069, both issued through the Science Mission Directorate. This material is also supported by the U.S. National Science Foundation under grant EAR-1753916.

Author contributions

J.C.R. performed the calculations and wrote the manuscript. J.K. designed the project, discussed the results, and commented on the manuscript.

Competing financial interests

The authors declare no competing financial interests.

Corresponding author

Correspondence and requests of computer code should be addressed to Juan Carlos Rosas (juanrb@cicese.mx) or Jun Korenaga (jun.korenaga@yale.edu).

Data availability

Data used for figures in the main text and Methods is generated by our convection and freeboard computer codes. We have been unable to share these data due to the significant size of the data files. Computer code to generate data files, however, is available upon request to J.C.R (juanrb@cicese.mx) or J.K (jun.korenaga@yale.edu).

Code availability

Computer code is available upon request to J.C.R (juanrb@cicese.mx) or J.K (jun.korenaga@yale.edu).

Figure #	Figure title One sentence only	Filename This should be the name the file is saved as when it is uploaded to our system. Please include the file extension. i.e.: *Smith_ED_Fi_1.jpg*	Figure Legend If you are citing a reference for the first time in these legends, please include all new references in the Online Methods References section, and carry on the numbering from the main References section of the paper.
Extended Data Fig. 1	Modeling Strategy	ext_fig1.pdf	Numerical results of a model with Ra=3x10^9 (η_0~1.3x10^{19} Pa s) and H*=13.2 (H=2.12x10^{-12} W kg^{-1}), appropriate for present-day Earth. **a-b**: Snapshots of uppermost section of temperature field at 40 Myr and 109 Myr, before and after onset of convection, respectively, with temperature contours at an interval of 100^o C. **c**: Horizontally-averaged temperature profiles for snapshots **a** and **b**. **d**: Ridge-perpendicular thermal structure constructed by assembling horizontally-averaged temperature profiles for every time step. Subsidence may then be calculated by computing instantaneous Stokes flow and applying Equation (1). Location of temperature profiles **a** and **b**, as well as the onset time, are shown. Isotherms of 1200^o C and 1300^o C as calculated using radiogenic heating (RH; solid) and half space cooling (HSC; dashed) bathymetries are highlighted. Prior to onset time, thermal structure of RH model resembles that predicted by HSC model.
Extended Data Fig. 2	Subsidence deviation	ext_fig2.pdf	**a**: Evolution of δw for models with different values of H* and $Ra = 3x10^8$. Models are divided into conductive and convective phases at onset time, with each phase being fitted by a linear trend (δw_1 and δw_2, respectively). For any H*, δw_1 intersects the horizontal axis at $t_i^{1/2} = 2.5$ Myr$^{1/2}$. **b-c**: Slope of δw_1 (**b**) and δw_2 at $t_{max} = 500$ Myr (**c**) as a function of H*. Linear trends are given by $m_1 = a_1 H^*$ in **b**, where $a_1 = 0.001$, and by $\delta w_2(t_{max}) = a_2 H^* + b_2$ in **c**, where $a_2 = 0.0228$ and $b_2 = 0.0452$. Color coding as in **a**.

Extended Data Fig. 3	Comparison between modeled bathymetry and empirical scaling law	ext_fig3.pdf	**a-c**: Modeled seafloor subsidence for models with $Ra = 3x10^8$ (**a**), $Ra = 1x10^9$ (**b**) and $Ra = 3x10^9$ (**c**), respectively (solid). Color coding as in Extended Data Figure 2. Seafloor subsidence as predicted from empirical scaling law is also shown (equation 16; dashed). **d-f**: Difference between modeled seafloor subsidence and empirical scaling for $a = 3x10^8$ (**d**), $Ra = 1x10^9$ (**e**) and $Ra = 3x10^9$ (**f**), respectively. Color coding as in **a**. Zero-difference level is shown (thin horizontal line). Difference never exceeds 250 m (dashed horizontal lines).

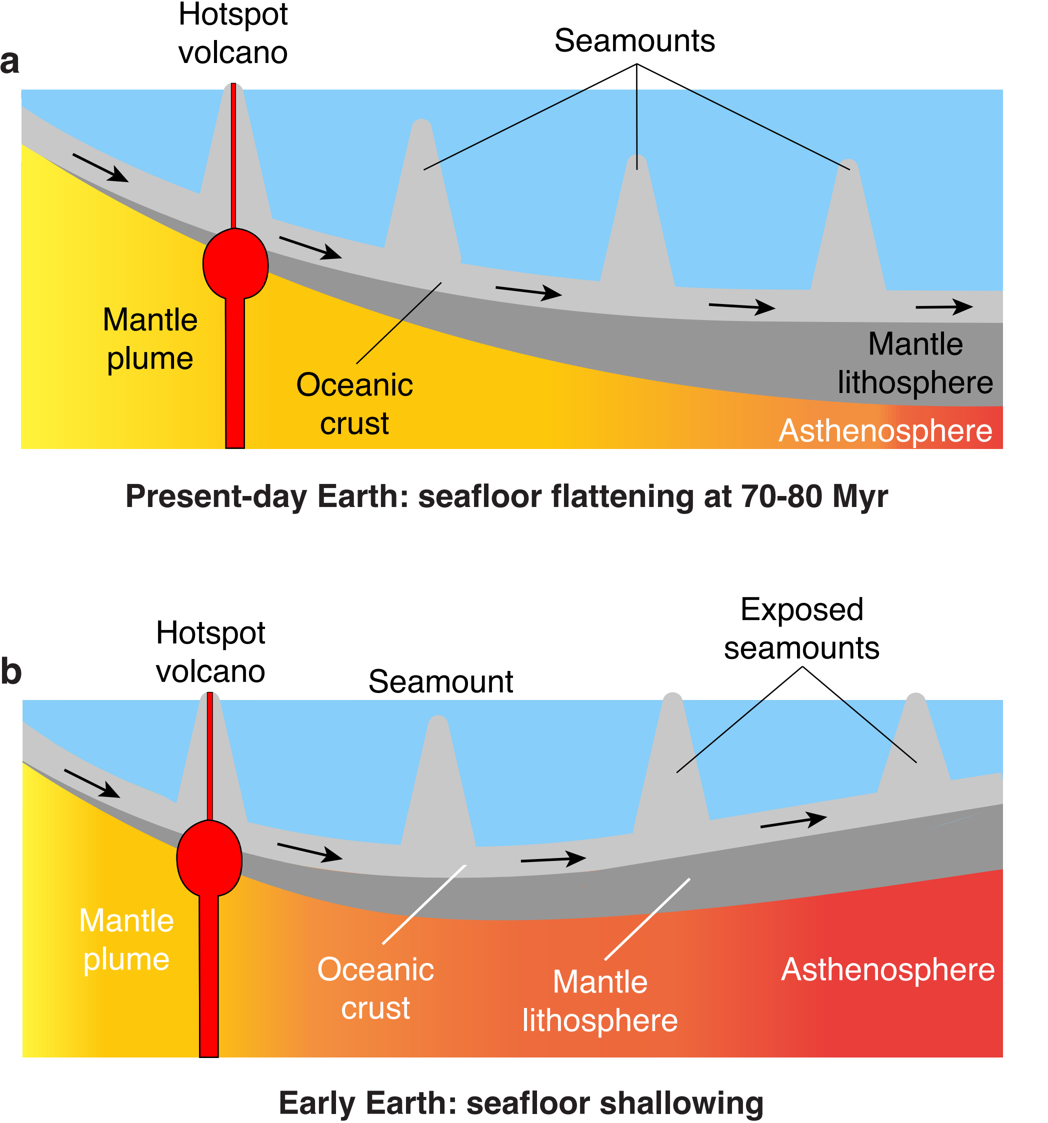
a
Hotspot volcano
Seamounts
Mantle plume
Oceanic crust
Mantle lithosphere
Asthenosphere
Present-day Earth: seafloor flattening at 70-80 Myr
b
Hotspot volcano
Seamount
Exposed seamounts
Mantle plume
Oceanic crust
Mantle lithosphere
Asthenosphere
Early Earth: seafloor shallowing

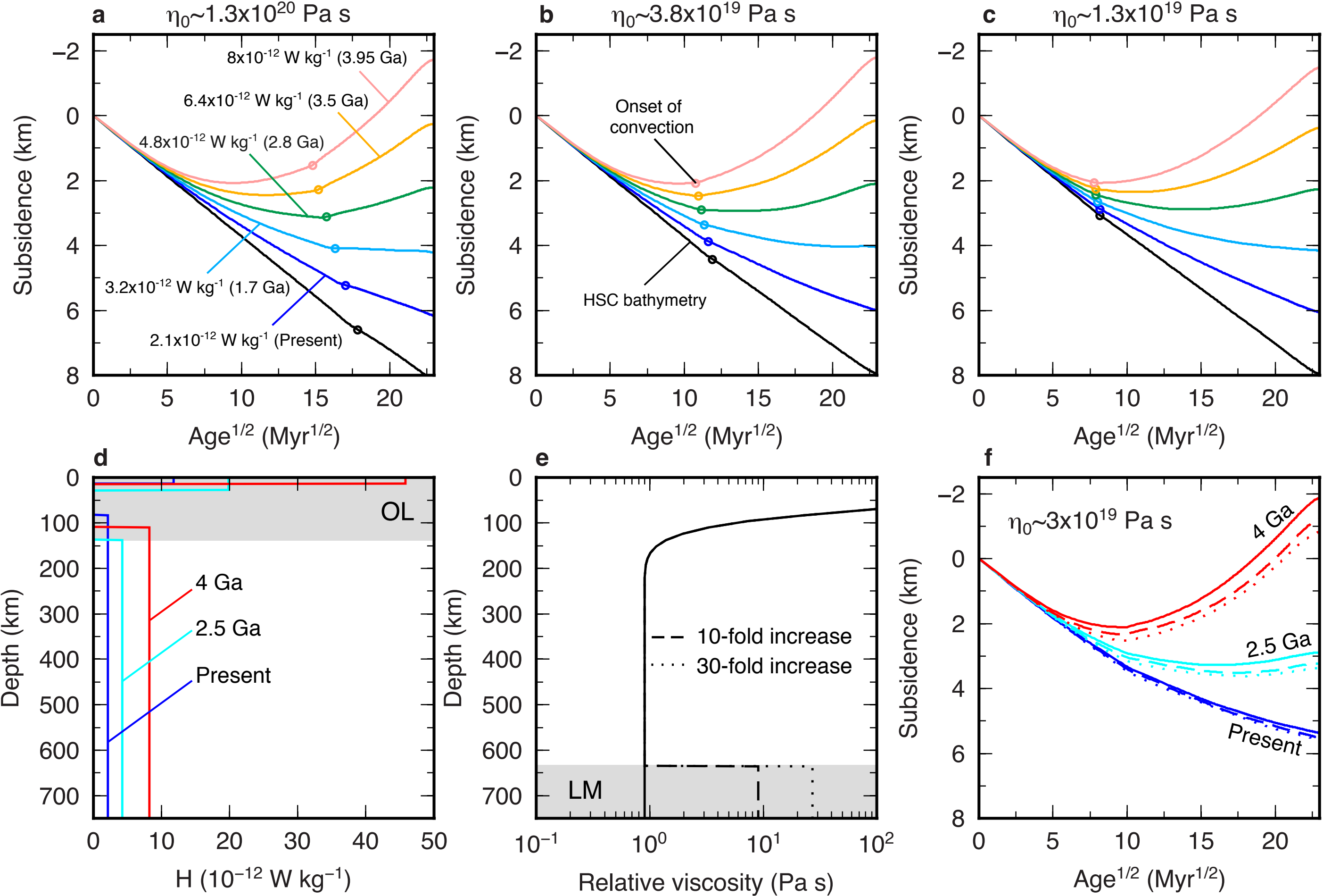

a
η_0~1.3x10^{20} Pa s
b
η_0~3.8x10^{19} Pa s
c
η_0~1.3x10^{19} Pa s
8x10^{-12} W kg^{-1} (3.95 Ga)
6.4x10^{-12} W kg^{-1} (3.5 Ga)
4.8x10^{-12} W kg^{-1} (2.8 Ga)
3.2x10^{-12} W kg^{-1} (1.7 Ga)
2.1x10^{-12} W kg^{-1} (Present)
Onset of convection
HSC bathymetry
Subsidence (km)
Age$^{1/2}$ (Myr$^{1/2}$)
d
OL
4 Ga
2.5 Ga
Present
Depth (km)
H (10^{-12} W kg^{-1})
e
10-fold increase
30-fold increase
LM
Relative viscosity (Pa s)
f
η_0~3x10^{19} Pa s
4 Ga
2.5 Ga
Present

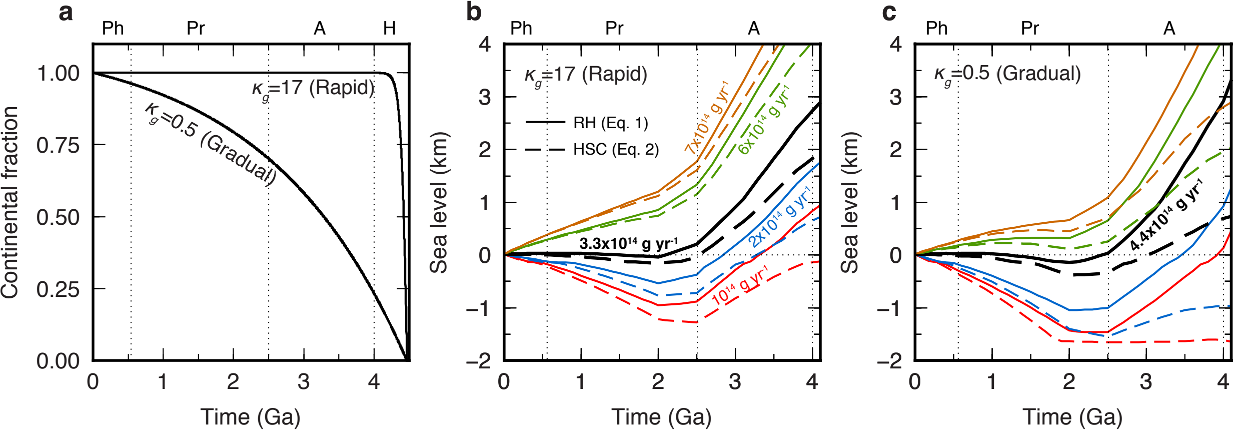

a
Ph
Pr
A
H
Continental fraction
1.00
0.75
0.50
0.25
0.00
κg=17 (Rapid)
κg=0.5 (Gradual)
0
1
2
3
4
Time (Ga)
b
Ph
Pr
A
Sea level (km)
κg=17 (Rapid)
RH (Eq. 1)
HSC (Eq. 2)
7x10^14 g yr^-1
6x10^14 g yr^-1
3.3x10^14 g yr^-1
2x10^14 g yr^-1
10^14 g yr^-1
Time (Ga)
c
Ph
Pr
A
Sea level (km)
κg=0.5 (Gradual)
4.4x10^14 g yr^-1
Time (Ga)

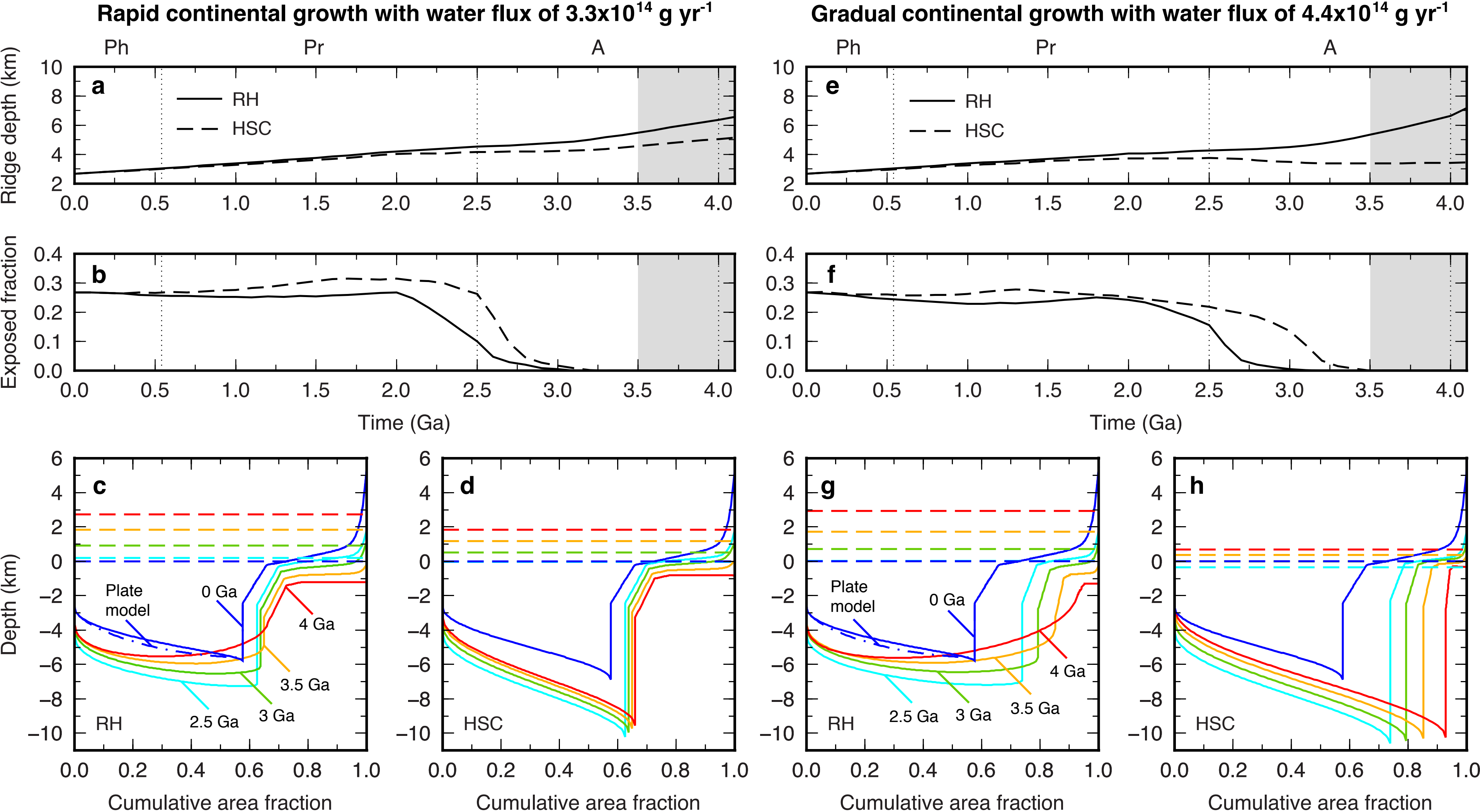

Rapid continental growth with water flux of 3.3x10^14 g yr^-1
Gradual continental growth with water flux of 4.4x10^14 g yr^-1
Ph
Pr
A
a
b
c
d
e
f
g
h
RH
HSC
Ridge depth (km)
Exposed fraction
Time (Ga)
Depth (km)
Cumulative area fraction
Plate model
0 Ga
2.5 Ga
3 Ga
3.5 Ga
4 Ga

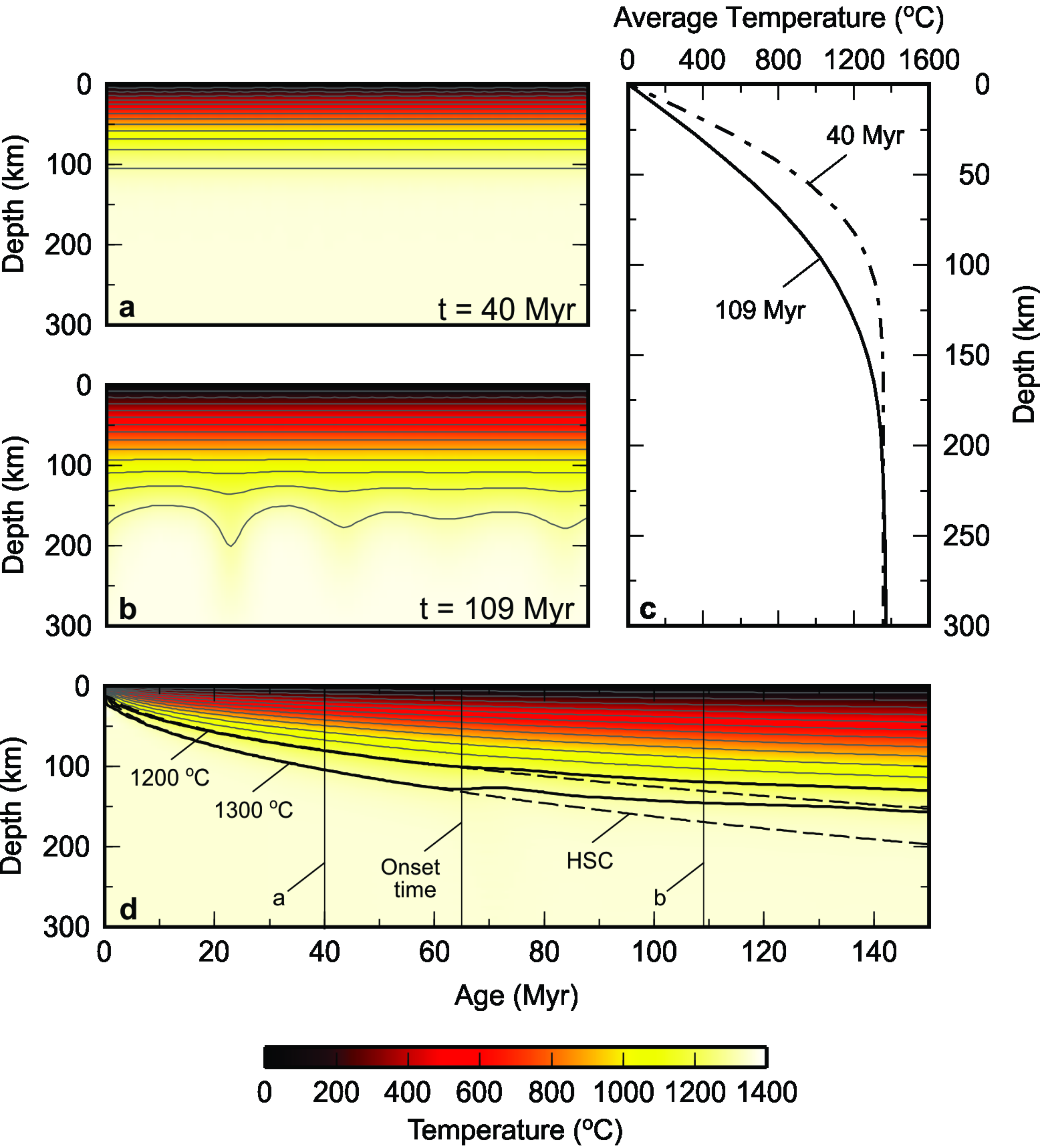

Average Temperature (°C)
0
400
800
1200
1600
40 Myr
109 Myr
Depth (km)
a
t = 40 Myr
b
t = 109 Myr
c
d
1200 °C
1300 °C
Onset time
HSC
Age (Myr)
Temperature (°C)
0
200
400
600
800
1000
1200
1400

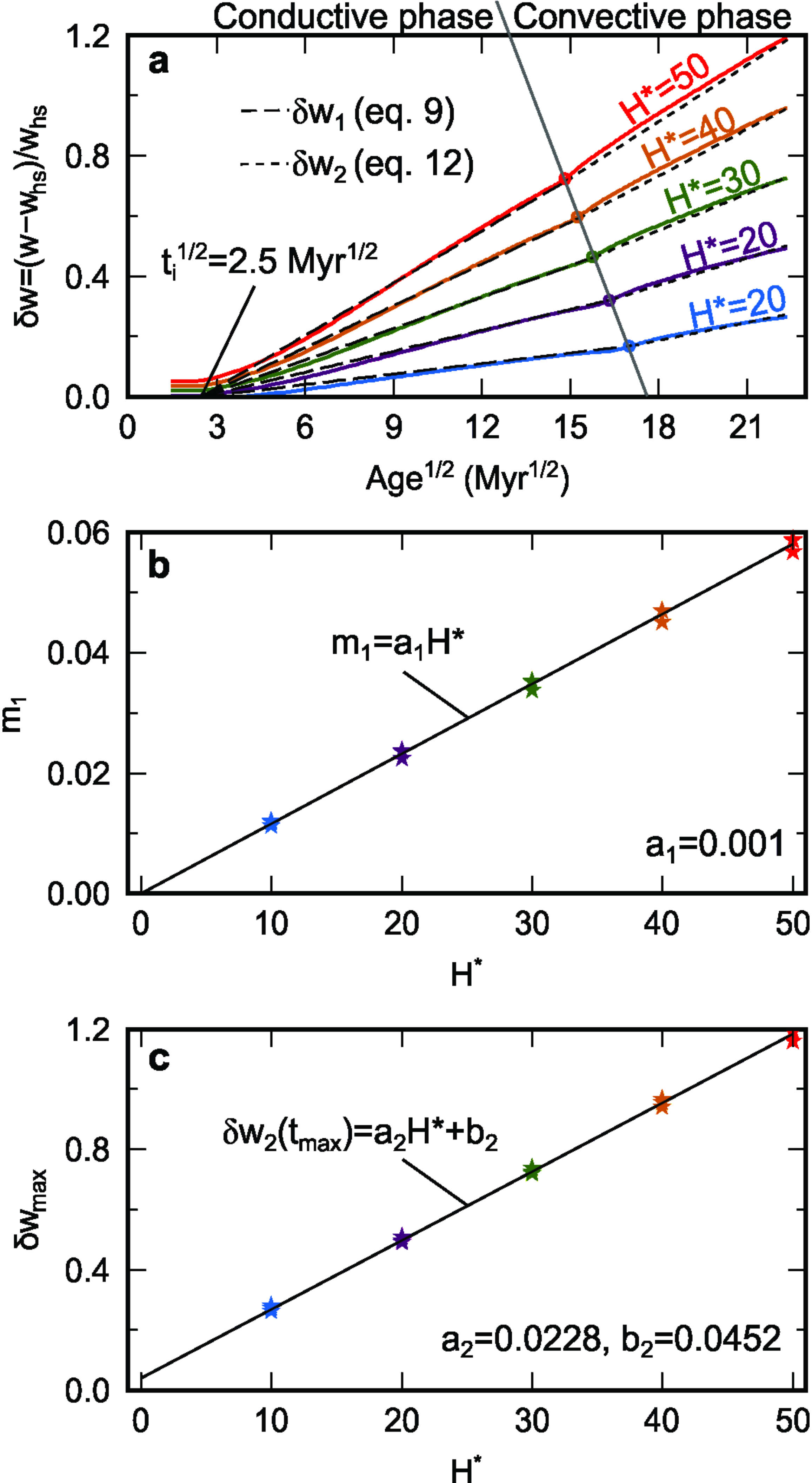

Conductive phase
Convective phase
a
δw=(w−w_hs)/w_hs
δw_1 (eq. 9)
δw_2 (eq. 12)
H*=50
H*=40
H*=30
H*=20
H*=20
t_i^1/2=2.5 Myr^1/2
Age^1/2 (Myr^1/2)
b
m_1
m_1=a_1H*
a_1=0.001
H*
c
δw_max
δw_2(t_max)=a_2H*+b_2
a_2=0.0228, b_2=0.0452
H*

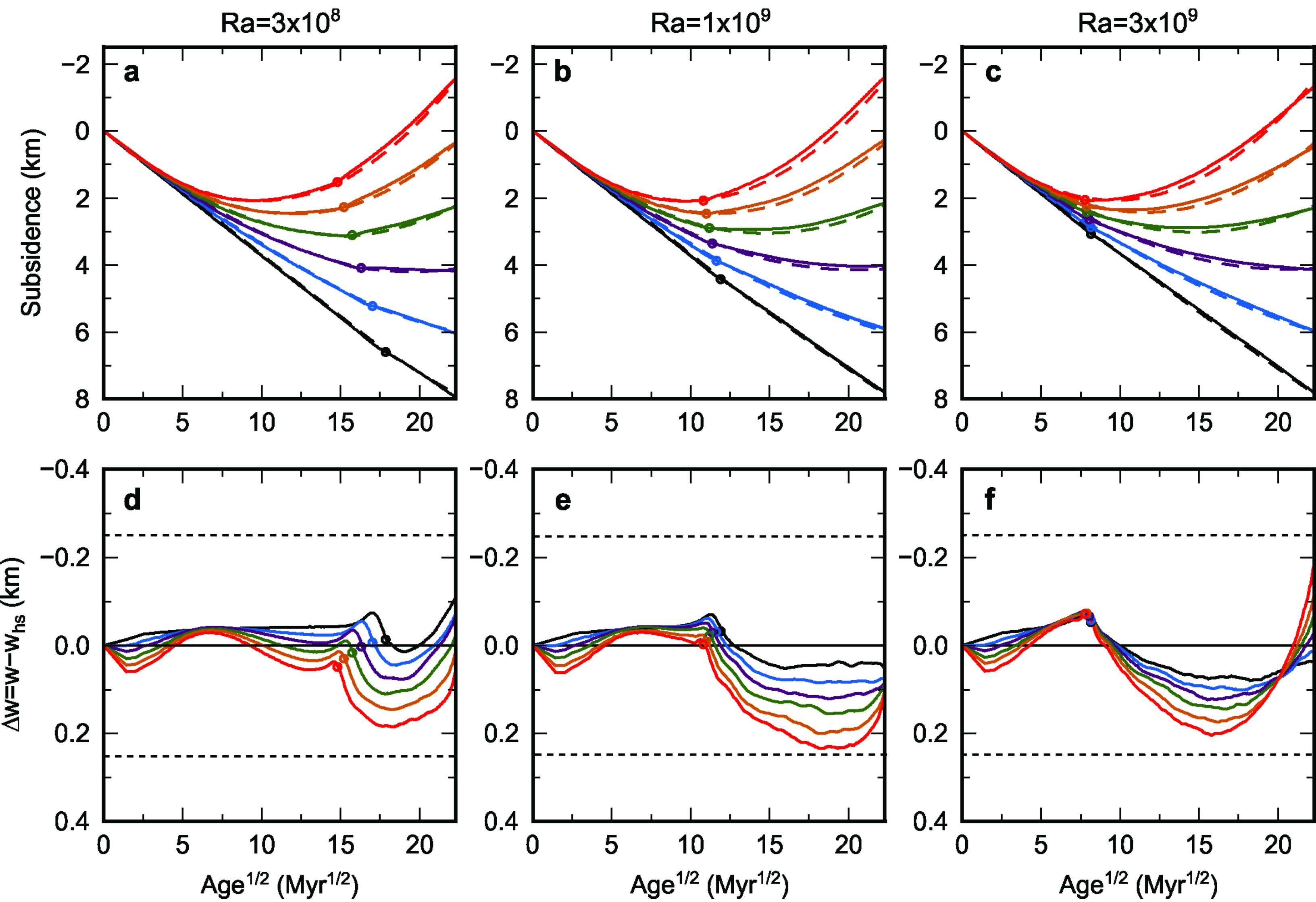

Ra=3x10^8
Ra=1x10^9
Ra=3x10^9
a
b
c
d
e
f
Subsidence (km)
Δw=w−w_hs (km)
Age^1/2 (Myr^1/2)